

Time-domain simulation of *SH*-wave-induced electromagnetic field in heterogeneous porous media: A fast finite-element algorithm

Qiyu Han* and Zhijing (Zee) Wang†

ABSTRACT

When a horizontally polarized rotational mechanical wave (*SH*-wave) travels through a porous rock, acceleration of the rock frame induces a streaming current in the *SH* particle motion plane. This streaming current is parallel to the particle displacement and has an associated electromagnetic (EM) field. This phenomenon is often described as the electroseismic (EOS) conversion. Numerically, the EOS phenomenon can be simulated in either the frequency or the time domain. Frequency-domain numerical simulation has huge memory and computational requirements. Traditional time-domain simulation, on the other hand, must restrict the time steps to be very small to satisfy stability conditions, resulting in large workload. In this paper, we present a fast finite-element (FE) method simulating the EOS conversion in the time domain. In our method, we decompose the large 2-D FE matrix equations into a set of 1-D matrix

equations and solve the problem using the approximate 1-D multistep process. We present numerical examples of 1-D and 2-D models to illustrate the coevolution of the seismic and electromagnetic fields.

Our simulation results show that the diffusive electrical field is induced from the spatial variations of mechanical and electrical properties of the porous media due to the imbalance of the induced electric current. Besides the direct *SH*-wave itself, the transmitted waves, multiple waves, reflected waves, and diffracted waves also induce diffusive electrical fields. The EOS conversion is potentially useful for reservoir characterization, but the EOS data may be difficult to interpret due to the complexity of the superposed wave fields. The diffusive nature of the induced EM fields suggests that antennas should be positioned close to the target of interest in in-situ measurements. As a result, borehole EOS surveys are likely to be more practical than surface surveys.

INTRODUCTION

Theoretical and experimental studies have demonstrated that electroseismic (EOS) phenomena in porous rocks could be used to detect oil reservoirs. Different physical mechanisms, such as piezoelectric and triboelectric effects and streaming currents have been proposed to explain these phenomena (Parkhomenko, 1971). Blau and Statham (1936) and Thompson (1936) conducted field experiments in which they applied a constant voltage to a pair of electrodes embedded in the ground and recorded the current modulation when seismic waves passed by the electrodes. In later experiments, Thompson (1939) showed that the current modulations were real and not caused by the change in contact resistance between the electrodes and the ground as a result of vibration. Ivanov (1939) discovered the EOS effect of the second kind by measuring electrical fields generated by seismic waves without applying any external voltage to the ground. Martner and

Sparks (1959) reported a systematic study of EOS coupling using explosives at various depths. Their results were the first to show that the conversion of seismic to electromagnetic (EM) energy at the water table could be detected using surface antennas. Thompson and Gist (1993) and Mikhailov et al. (1997) also made field measurements which demonstrated that seismic waves could induce EM disturbances in saturated sediments.

Many theoretical studies of the EOS phenomenon have been carried out. For example, Frenkel (1944) postulated equations for estimating the amount of relative fluid-solid motion induced by a seismic wave. Pride (1994) volume-averaged the continuum equations that have the form of Maxwell's equations coupled with Biot's (1956) equations. Han (1995, 1997) studied the feasibility of using the EOS effects for reservoir exploration. He derived a set of equations considering several mechanisms that can cause coupling between seismic and EM energies in fluid-saturated rocks, including changes of electrical

Manuscript received by the Editor November 03, 1998; revised manuscript received May 12, 2000.

*Department of Geo-resources, University of Petroleum (East China), Dongying 257062, Shandong, China. E-mail: qiyuhan@sltx.com.cn.

†Chevron Petroleum Technology Company, RM-D1124, P.O. Box 6019, San Ramon, California 94583-0719. E-mail: zwan@chevron.com.

© 2001 Society of Exploration Geophysicists. All rights reserved.

resistivity and electrolyte concentration due to volume changes of the pore fluid and the rock frame.

Numerical modeling based on EOS theories provides a means for understanding and interpreting the EOS phenomenon in heterogeneous media. The rapid decay of the EM fields and their vector nature makes it difficult to simulate the EOS fields. With the analytical Green's function, Pride and Haartsen (1996) and Mikhailov et al. (1997) obtained eigenvector solutions in the frequency-wave number (f - k) domain in porous media, which can be used to simulate layered media. However, it is difficult to derive eigenvector solutions of highly heterogeneous media in the f - k domain with the analytical Green's function method.

Numerical methods, such as the finite-element (FE) and the finite-difference (FD) methods, can model highly heterogeneous media in either the time or frequency domain. Frequency-domain methods are better than time-domain methods in terms of accuracy (Marfurt, 1984), so that they are invaluable in crosshole seismic imaging (Pratt, 1990; Pratt and Worthington, 1990; Song and Williamson, 1995). However, they require large amounts of memory and computational effort because of the large, complex-valued coefficient matrices and double precision arithmetic operations (Gu, 1985; Pratt, 1990). In the time domain, explicit traditional methods must restrict the time steps to be very small to satisfy stability conditions (Oristaglio and Hohmann, 1984), and therefore are not feasible for modeling the coevolution of the seismic EM fields.

In this paper, we present a time-domain FE algorithm to model the 2-D coupled fields. In this algorithm, the FE matrix equation of the EM field is unconditionally stable. In addition, we decompose the large FE matrix equations into a set of uncoupled tridiagonal matrix equations with only 1-D orders to solve the 2-D problem in 1-D. The algorithm significantly reduces memory storage and computing time so that it is suitable for simulating the time-domain evolution of the *SH*-wave-induced, diffusive EM field in highly heterogeneous porous media.

SH-WAVE EOS EQUATIONS

Electrokinetic phenomena are usually studied with respect to solid-liquid interfaces. When two phases of different chemical composition are in contact, an electric potential difference develops at the interface. The anions from the electrolyte are absorbed to the solid interface leaving behind a net excess of cations distributed near the wall, producing an electrical double layer. There are several models of the electric double layer, one of which is the diffuse layer Gouy-Chapman model (Bockris and Reddy, 1970; Dukhin and Derjaguin, 1974), where the ions are attracted to the surface only by electrostatic forces. Another model of the solid-fluid interface is that the electrolyte ions and structured water molecules are not only electrostatically but also chemically absorbed to the surface of the solid (Pride and Morgan, 1991). If no externally superposed EM fields exist, the 2-D time-domain vector equations relating the conservation equations for fluid flow and current flow are (Pride, 1994),

$$\mathbf{J} = \sigma_s \mathbf{E} - L((\partial_x P \hat{\mathbf{x}} + \partial_z P \hat{\mathbf{z}}) + \rho_f \partial_{tt} \mathbf{u}), \quad (1)$$

and

$$\partial_t \mathbf{W} = L \mathbf{E} - \frac{k}{\eta} (\partial_x P \hat{\mathbf{x}} + \partial_z P \hat{\mathbf{z}} + \rho_f \partial_{tt} \mathbf{u}), \quad (2)$$

where \mathbf{u} is the displacement vector of the rock matrix, \mathbf{W} is the displacement vector of the fluid relative to that of the solid, \mathbf{E} is the induced electric field vector, \mathbf{J} is the electrical current density vector, P is the hydraulic potential, σ_s is the electric conductivity of the fluid-saturated porous medium, L is the current crosscoupling coefficient linking hydraulic and electrical transport processes, k is the permeability of the porous medium, η is the viscosity of the pore fluid, and ρ_f is the density of the pore fluid.

Conductivity of the fluid-saturated porous medium can be estimated from Archie's law (Archie, 1942): $\sigma_s = \sigma_f \phi^c$, where σ_f is the conductivity of the saturating fluid, ϕ is the porosity, and c is the cementation exponent. For reservoir sandstones, cementation exponents commonly range from 1.6 to 2.0 (Sprunt et al., 1990). The current crosscoupling coefficient takes account of both actions of the electric field and the fluid pressure on the charge density. Pride (1994) derived a frequency-dependent function of the coupling coefficient. At low frequencies, Pride's definition is given by

$$L \approx L_0 = -\frac{\phi}{\alpha_\infty} \frac{\varepsilon_f k \zeta}{\eta} \left(1 - 2 \frac{\tilde{d}}{R} \right), \quad (3)$$

where $\zeta = 0.008 + 0.026 \log_{10}(C)$ is the zeta potential (Pride and Morgan, 1991) with C being the electrolyte concentration, α_∞ is the tortuosity that can be determined by Berryman's method (Berryman, 1980) using $\alpha_\infty = 1 - F(1 - 1/\phi)$, where ϕ is porosity and F is a factor dependent on the microscopic pore shape or geometry; R is the pore radius of the porous medium; ε_f is the dielectric permittivity of the fluid; $\tilde{d} = \frac{3 \times 10^{-10}}{\sqrt{C}}$ is the Debye length in meters.

The first term on the right-hand side of equation (1) is the conduction current and the second term is the streaming current. The first term on the right-hand side of equation (2) describes the amount of fluid flow caused by the electric field. If this term is ignored, equation (2) expresses only the dynamic primary flow, which gives rise to the electrokinetic phenomenon. In the absence of external current sources, the first term on the right-hand side of equation (2) denotes a feedback coupling of the electrokinetic process, which is small for geological media (Fitterman, 1978). Equation (2) can be rewritten as

$$L(\partial_x P \hat{\mathbf{x}} + \partial_z P \hat{\mathbf{z}} + \rho_f \partial_{tt} \mathbf{u}) = \frac{L^2 \eta}{k} \mathbf{E} - \frac{L \eta}{k} \partial_t \mathbf{W}. \quad (4)$$

Substituting equation (4) into equation (1), we obtain

$$\mathbf{J} = \mathbf{J}_c + \mathbf{J}_s, \quad (5)$$

where $\mathbf{J}_c = \sigma \mathbf{E}$, $\sigma = \sigma_s - \frac{L^2 \eta}{k}$, and $\mathbf{J}_s = \frac{L \eta}{k} \partial_t \mathbf{W}$.

Equation (5) describes that the total current density is composed of a source current density \mathbf{J}_s caused by charges moved by seismic waves, and a conduction current density \mathbf{J}_c caused by the effective conductivity σ ; σ is determined by the electrolytic conduction and the EOS coupling.

When a horizontally polarized *SH*-wave propagates through a porous medium, the wave causes divergence-free grain

accelerations and relative motion between the fluid and solid grains. The relative motion generates a sheetlike current that acts as a source in Ampere's law and induces a transverse electrical (TE) field parallel to the seismic particle displacement (Pride and Haartsen, 1996). The induced TE field propagates with the *SH*-wave speed. The *SH*-wave can only generate currents in the *SH* particle motion plane in homogeneous isotropic poroelastic media. In this case, Maxwell's equations reduce to a scalar damped wave equation. EM diffusion can be described by the loss tangent, $\tan \delta = \sigma/\omega\epsilon$, where ϵ is the dielectric permittivity of the medium and ω is the angular frequency. For frequencies encountered in seismic wave propagations in the earth, $\tan \delta > 1$, i.e., diffusion dominates. The damped wave equation then reduces to a diffusion equation,

$$\partial_{xx}E + \partial_{zz}E - \sigma\mu_0\partial_t E = S_e, \quad (6)$$

where S_e is the source term equal to $\mu_0\partial_t J_s$, and μ_0 is the magnetic permeability which is assumed to be constant and equal to its free-space value $4\pi \times 10^{-7}$ H/m.

Equation (6) has an analytical Green's function solution for a point source. The homogeneous isotropic whole-space 2-D Green's function for equation (6) is the solution of

$$\partial_{xx}G + \partial_{zz}G - \sigma\mu_0\partial_t G = -\mu_0I\delta(x)\delta(z)\delta(t), \quad (7)$$

and is given by

$$G(x, z, t) = \frac{\mu_0 I}{4\pi t} e^{-\mu_0 \sigma R^2/4t}, \quad (8)$$

where $R = (x^2 + z^2)^{1/2}$ is the distance from the delta function source with amplitude $-\mu_0 I$ (Wolf, 1979).

In this paper, we use Biot's shear wave equations (Biot, 1962) to simulate the *SH*-wave field in a two-phase medium. The seismic EOS coupling equations are

$$\mu\partial_{xx}u + \mu\partial_{zz}u - \partial_{tt}(\rho u + \rho_f W) = 0, \quad (9)$$

$$\partial_{tt}(\rho_f u + mW) + \frac{\eta}{k}\partial_t W = 0, \quad (10)$$

$$\partial_{xx}E + \partial_{zz}E - \mu_0\sigma\partial_t E - S = 0, \quad (11)$$

where $S = \frac{\mu_0\eta L}{k}\partial_{tt}W$ is the effective EOS source term, u is the y -component of the solid material displacement, W is the displacement of the fluid relative to that of the solid, $m = \alpha_\infty\rho_f/\phi$ is the effective fluid density, μ is the shear modulus of the dry medium, $\rho = \phi\rho_f + (1 - \phi)\rho_s$ is the overall density of the saturated medium, and ρ_s is the density of the solid matrix of the porous medium.

FE SOLUTION OF THE PROBLEM

Variational equations

Given a plane domain S with boundary ∂S , $\bar{S} = S \cup \partial S$. Suppose matrix $\mathbf{V} = \begin{pmatrix} u \\ W \end{pmatrix}$ is a solution of equation (9) combined with equation (10) and E is a solution of equation (11), E and $\mathbf{V} \in C^1(\bar{S}) \cap C^2(S)$. For all E and $\mathbf{V} \in \{\mathbf{V} \mid \mathbf{V} \in C^1(\bar{S}), \mathbf{V}|_{\partial S} = 0\}$,

$$\iint_S \mathbf{L}\mathbf{V} \mathbf{v} dx dz = \mathbf{0}, \quad (12)$$

$$\iint_S (\partial_{xx}E + \partial_{zz}E - \mu_0\sigma\partial_t E - S)v_E dx dz = 0, \quad (13)$$

where matrix

$$\mathbf{v} = \begin{pmatrix} v_u \\ v_W \end{pmatrix}$$

and matrix

$$\mathbf{L} = \begin{pmatrix} \mu\nabla^2 - \rho\partial_{tt} & -\rho_f\partial_{tt} \\ \rho_f\partial_{tt} & m\partial_{tt} + \frac{\eta}{k}\partial_t \end{pmatrix}.$$

Equations (12) and (13) can be rewritten as

$$\iint_S \begin{pmatrix} \mu\nabla^2uv_u - \rho\partial_{tt}uv_u - \rho_f\partial_{tt}Wv_W \\ \rho_f\partial_{tt}uv_u + m\partial_{tt}Wv_W + \frac{\eta}{k}\partial_t Wv_W \end{pmatrix} dx dz = \begin{pmatrix} 0 \\ 0 \end{pmatrix}, \quad (14)$$

$$\iint_S (\partial_{xx}Ev_E + \partial_{zz}Ev_E - \mu_0\sigma\partial_tE v_E - Sv_E) dx dz = 0. \quad (15)$$

With Green's formula and integration by parts, considering boundary condition $\mathbf{V}|_{\partial S} = 0$ and $E|_{\partial S} = 0$, i.e., $\int_{\partial S} v_u \frac{\partial u}{\partial n} d\ell = 0$, $\int_{\partial S} v_W \frac{\partial W}{\partial n} d\ell = 0$, and $\int_{\partial S} v_E \frac{\partial E}{\partial n} d\ell = 0$, where $d\ell$ is the length element, we obtain the Galerkin variation formulations of the seismic problem, i.e., finding solutions of u , W and E that satisfy the following equations

$$\iint_S (\mu\nabla u \cdot \nabla v_u + \rho\partial_{tt}uv_u + \rho_f\partial_{tt}Wv_W) dx dz = 0, \quad (16)$$

$$\iint_S \left(-\rho_f\partial_{tt}uv_u - m\partial_{tt}Wv_W - \frac{\eta}{k}\partial_t Wv_W \right) dx dz = 0, \quad (17)$$

$$\iint_S (\nabla E \cdot \nabla v_E + \mu_0\sigma\partial_{tt}Ev_E + Sv_E) dx dz = 0. \quad (18)$$

Equations (9) through (11) can be approximately represented by the variational formulas (16)–(18) with which we can obtain the weak solutions of equations (9)–(11).

FE equations

Discretization of equations (16)–(18) is limited in a rectangular domain S . Choosing the Cartesian coordinate system, we divide the 2-D solution domain S into a set of rectangular elements. The numbers of the nodal points in the x - and z -directions are m and n , respectively. The overall number of the nodes is $l = m \times n$. In addition, we assume L_x and L_z to be 1-D solution domain in the x - and z -directions, respectively. Employing linear interpolation functions (Lu and Guan, 1987)

$$\omega_i(x) = \begin{cases} (x - x_{i-1})/(x_i - x_{i-1}), & x \in [x_{i-1}, x_i] \\ (x_{i+1} - x)/(x_{i+1} - x_i), & x \in [x_i, x_{i+1}] \\ 0, & \text{otherwise} \end{cases} \quad (i = 1, 2, \dots, m), \quad (19)$$

$$\omega_k(z) = \begin{cases} (z - z_{k-1})/(z_k - z_{k-1}), & z \in [z_{k-1}, z_k] \\ (z_{k+1} - z)/(z_{k+1} - z_k), & z \in [z_k, z_{k+1}] \\ 0, & \text{otherwise} \end{cases} \quad (20)$$

and defining tensors

$$\hat{\omega}(x) = (\omega_1(x), \omega_2(x), \dots, \omega_m(x)),$$

$$\hat{\omega}(z) = (\omega_1(z), \omega_2(z), \dots, \omega_n(z)),$$

$$\hat{\omega}(x, z) = \hat{\omega}(x) \otimes \hat{\omega}(z),$$

where \otimes means the tensor product. We can approximate the solution of seismic and electric fields at time t as

$$\hat{\mathbf{V}}(x, z) = \hat{\omega}(x, z) \cdot \hat{\mathbf{V}}^t, \quad (21)$$

where tensors $\hat{\mathbf{V}}^t = (V_1^t, V_2^t, \dots, V_l^t)^T$ and $V_j^t = E_j^t, u_j^t$, or W_j^t , ($j = 1, \dots, l$).

With the variational formulas and equation (21) and replacing the derivative at $t = q\Delta t$ by the forward difference between the values taken at $(q+1)\Delta t$ and $q\Delta t$, we obtain the FE matrix equations

$$\mathbf{W}^{q+1} = \Lambda_1 \mathbf{W}^q - \Lambda_2 \mathbf{W}^{q-1} + \Lambda_3 \mathbf{P} \Lambda_4 \mathbf{u}^q, \quad (22)$$

$$\begin{aligned} \mathbf{u}^{q+1} = & 2\mathbf{u}^q + \mathbf{u}^{q-1} - \Lambda_5 \mathbf{W}^{q+1} + 2\Lambda_5 \mathbf{W}^q \\ & - \Lambda_5 \mathbf{W}^{q-1} - \Lambda_6 \mathbf{P} \Lambda_4 \mathbf{u}^q, \end{aligned} \quad (23)$$

$$\mathbf{M} \Lambda_7 (\mathbf{E}^{q+1} - \mathbf{E}^q) + \mathbf{K} \mathbf{E}^q = \mathbf{M} \mathbf{S}^q, \quad (24)$$

where \mathbf{M} and \mathbf{K} are mass and stiffness matrices related to the basis functions $\hat{\omega}(x, z)$ as

$$\begin{aligned} \mathbf{M} &= \iint_S \hat{\omega}^T \cdot \hat{\omega} dx dz \\ &= \int_{L_x} \hat{\omega}^T(x) \cdot \hat{\omega}(x) dx \otimes \int_{L_z} \hat{\omega}^T(z) \cdot \hat{\omega}(z) dz \\ &= \mathbf{M}_x \otimes \mathbf{M}_z, \\ \mathbf{K} &= \iint_S (\partial_x \hat{\omega}^T \cdot \partial_x \hat{\omega} + \partial_z \hat{\omega}^T \cdot \partial_z \hat{\omega}) dx dz \\ &= \mathbf{K}_x \otimes \mathbf{M}_z + \mathbf{M}_x \otimes \mathbf{K}_z, \end{aligned}$$

and \mathbf{P} is given by

$$\mathbf{P} = \mathbf{M}_x^{-1} \mathbf{K}_x \otimes \mathbf{I}_z + \mathbf{I}_x \otimes \mathbf{M}_z^{-1} \mathbf{K}_z,$$

where

$$\mathbf{K}_x = \int_{L_x} \partial_x \hat{\omega}^T(x) \cdot \partial_x \hat{\omega}(x) dx,$$

$$\mathbf{K}_z = \int_{L_z} \partial_z \hat{\omega}^T(z) \cdot \partial_z \hat{\omega}(z) dz.$$

Matrices \mathbf{M} and \mathbf{K} are $(m \times n) \times (m \times n)$ banded matrices. Matrices \mathbf{M}_x and \mathbf{K}_x are $m \times m$ tridiagonal matrices, and \mathbf{I}_x is unitary matrix of order m . \mathbf{M}_z and \mathbf{K}_z are $n \times n$ tridiagonal matrices, and \mathbf{I}_z is unitary matrix of order n . For all $i = 1, \dots, m$ and $k = 1, \dots, n$, the elements of the diagonal matrices $\Lambda_1 - \Lambda_7$ are

$$\begin{aligned} \Lambda_1^{ik} &= \frac{4K^{ik}(m\rho^{ik} - \rho_f^{ik}\rho_f^{ik})}{2K^{ik}m\rho^{ik} - 2K^{ik}\rho_f^{ik}\rho_f^{ik} + \Delta t\eta^{ik}\rho^{ik}}, \\ \Lambda_2^{ik} &= \frac{2K^{ik}m\rho^{ik} - 2K^{ik}\rho_f^{ik}\rho_f^{ik} - \Delta t\eta^{ik}\rho^{ik}}{2K^{ik}m\rho^{ik} - 2K^{ik}\rho_f^{ik}\rho_f^{ik} + \Delta t\eta^{ik}\rho^{ik}}, \\ \Lambda_3^{ik} &= \frac{2K^{ik}\rho_f^{ik}\Delta t^2}{2K^{ik}m\rho^{ik} - 2K^{ik}\rho_f^{ik}\rho_f^{ik} + \Delta t\eta^{ik}\rho^{ik}}, \\ \Lambda_4^{ik} &= \mu^{ik}, \\ \Lambda_5^{ik} &= \frac{\rho_f^{ik}}{\rho^{ik}}, \\ \Lambda_6^{ik} &= \frac{\Delta t^2}{\rho^{ik}}, \\ \Lambda_7^{ik} &= \frac{\mu_0\sigma^{ik}}{\Delta t}. \end{aligned}$$

The Crank-Nicolson scheme (Goldman et al., 1986) is chosen to obtain an unconditionally stable algorithm for solving the converted electric field. By substituting the second term \mathbf{KE}^q on the left-hand side of equation (24) for $\mathbf{K}[\theta \mathbf{E}^{q+1} + (1-\theta)\mathbf{E}^q]$ and the source term \mathbf{MS}^q for $\mathbf{M}[\theta \mathbf{S}^{q+1} + (1-\theta)\mathbf{S}^q]$, we obtain the FE matrix equation

$$(\mathbf{I} + \mathbf{P}_1) \mathbf{E}^{q+1} = (\mathbf{I} - \mathbf{P}_2) \mathbf{E}^q + \mathbf{R}^q, \quad (25)$$

where $\mathbf{P}_1 = \mathbf{P}_{x1} + \mathbf{P}_{z1}$, $\mathbf{P}_2 = \mathbf{P}_{x2} + \mathbf{P}_{z2}$, $\mathbf{P}_{x1} = \Lambda_{E1}^{-1}(\mathbf{M}_x^{-1} \mathbf{K}_x \otimes \mathbf{I}_z)$, $\mathbf{P}_{x2} = \Lambda_{E2}^{-1}(\mathbf{M}_x^{-1} \mathbf{K}_x \otimes \mathbf{I}_z)$, $\mathbf{P}_{z1} = \Lambda_{E1}^{-1}(\mathbf{I}_x \otimes \mathbf{M}_z^{-1} \mathbf{K}_z)$, $\mathbf{P}_{z2} = \Lambda_{E2}^{-1}(\mathbf{I}_x \otimes \mathbf{M}_z^{-1} \mathbf{K}_z)$, $\mathbf{R}^q = \Lambda_{E1}^{-1} \mathbf{S}^{q+1} + \Lambda_{E2}^{-1} \mathbf{S}^q$, $\Lambda_{E1}^{-1} = \theta \Lambda_7^{-1}$, $\Lambda_{E2}^{-1} = (1-\theta) \Lambda_7^{-1}$, and $\mathbf{I} = \mathbf{I}_x \otimes \mathbf{I}_z = \mathbf{I}_z \otimes \mathbf{I}_x$.

Matrix equation (25) is accurate to the first order in Δt for $\theta \neq 1/2$ and to the second order for $\theta = 1/2$. It is stable for $1/2 \leq \theta \leq 1$.

Enormous memory storage and extensive computing time are needed to solve equations (22), (23), and (25) directly because \mathbf{M} and \mathbf{K} are banded large matrices. To avoid dealing with large matrices, we develop an approximate multistep 1-D algorithm. We only need to solve a set of tridiagonal matrix equations in each step. In doing so, we obtain, after some algebra, the final form of the matrix system:

$$\mathbf{W}^{q+1} = \Lambda_1 \mathbf{W}^q - \Lambda_2 \mathbf{W}^{q-1} + \Lambda_3 \mathbf{P} \Lambda_4 \mathbf{u}^q, \quad (26)$$

$$\begin{aligned} \mathbf{u}^{q+1} = & 2\mathbf{u}^q + \mathbf{u}^{q-1} - \Lambda_5 \mathbf{W}^{q+1} + 2\Lambda_5 \mathbf{W}^q \\ & - \Lambda_5 \mathbf{W}^{q-1} - \Lambda_6 \mathbf{P} \Lambda_4 \mathbf{u}^q, \end{aligned} \quad (27)$$

$$(\mathbf{I} + \mathbf{P}_{x1})(\mathbf{I} + \mathbf{P}_{z1}) \mathbf{E}^{q+1} = (\mathbf{I} - \mathbf{P}_2) \mathbf{E}^q + \mathbf{R}^q. \quad (28)$$

The error caused by substituting matrix equation (28) for equation (25) is $\mathbf{P}_{x1} \mathbf{P}_{z1} \mathbf{E}^{q+1}$, which is related to $\Delta x, \Delta z, \Delta t, \sigma(x, z)$,

and the grid number of a mesh. We will discuss this in a later section.

THE APPROXIMATE 1-D FE ALGORITHM

The major workload in solving equations (26)–(28) is computing the terms $\Lambda_3 \mathbf{P} \Lambda_4 \mathbf{u}^q$, $\Lambda_6 \mathbf{P} \Lambda_4 \mathbf{u}^q$, $\mathbf{P}_2 \mathbf{E}^q$, and $(\mathbf{I} + \mathbf{P}_{x1})(\mathbf{I} + \mathbf{P}_{z1}) \mathbf{E}^{q+1} = \bar{\mathbf{E}}$, where $\bar{\mathbf{E}}$ denotes summation of the terms on the right-hand side of equation (28). The terms $\Lambda_3 \mathbf{P} \Lambda_4 \mathbf{u}^q$, $\Lambda_6 \mathbf{P} \Lambda_4 \mathbf{u}^q$, and $\mathbf{P}_2 \mathbf{E}^q$ have similar form $\mathbf{P}\mathbf{U}$, where $\mathbf{U} = (U_1, \dots, U_l)^T$ denotes $\Lambda_4 \mathbf{u}^q$, $\Lambda_6 \mathbf{u}^q$, or \mathbf{E}^q , so that we can use the same algorithm to compute them. The term $\mathbf{P}\mathbf{U}$ consists of two parts: $(\mathbf{M}_x^{-1} \mathbf{K}_x \otimes \mathbf{I}_z) \mathbf{U}$ and $(\mathbf{I}_x \otimes \mathbf{M}_z^{-1} \mathbf{K}_z) \mathbf{U}$. Suppose matrix $\bar{\mathbf{U}} = (\bar{U}_1, \dots, \bar{U}_l)^T$ represents $(\mathbf{M}_x^{-1} \mathbf{K}_x \otimes \mathbf{I}_z) \mathbf{U}$ and matrix $\mathbf{A} = \mathbf{M}_x^{-1} \mathbf{K}_x$, according to the definition of tensor product, we obtain

$$(\mathbf{A} \otimes \mathbf{I}_z) \mathbf{U} = \bar{\mathbf{U}}, \quad (29)$$

which can be rewritten as

$$\begin{aligned} & \left[\begin{array}{ccccccccc} a_{11} & \cdots & 0 & \cdots & a_{1m} & \cdots & 0 \\ \vdots & \ddots & \vdots & \cdots & \vdots & \ddots & \vdots \\ 0 & \cdots & a_{11} & \cdots & 0 & \cdots & a_{1m} \\ \vdots & \vdots & \vdots & \ddots & \vdots & \vdots & \vdots \\ a_{m1} & \cdots & 0 & \cdots & a_{mm} & \cdots & 0 \\ \vdots & \ddots & \vdots & \cdots & \vdots & \ddots & \vdots \\ 0 & \cdots & a_{m1} & \cdots & 0 & \cdots & a_{mm} \end{array} \right]_{l \times l} \\ & \times \begin{bmatrix} U_1 \\ U_2 \\ \vdots \\ U_l \end{bmatrix} = \begin{bmatrix} \bar{U}_1 \\ \bar{U}_2 \\ \vdots \\ \bar{U}_l \end{bmatrix}. \end{aligned} \quad (30)$$

The $l \times l$ matrix equation (30) is equivalent to a set of $m \times m$ matrix equations

$$\mathbf{A}\mathbf{U}^k = \bar{\mathbf{U}}^k, \quad (k = 1, 2, \dots, n), \quad (31)$$

where matrices $\mathbf{U}^k = (U_1^k, \dots, U_m^k)^T$ and $\bar{\mathbf{U}}^k = (\bar{U}_1^k, \dots, \bar{U}_m^k)^T$, ($k = 1, 2, \dots, n$), whose elements are along the x -direction, can be considered as a set of x -domain matrices of \mathbf{U} and $\bar{\mathbf{U}}$, respectively, corresponding to the point k in the z -domain. After some algebra, we write matrix equations (31) as the following multistep process:

$$\mathbf{M}_x \bar{\mathbf{U}}^k = \mathbf{K}_x \mathbf{U}^k. \quad (k = 1, 2, \dots, n). \quad (32)$$

Suppose matrix $\bar{\mathbf{U}} = (\bar{U}_1, \dots, \bar{U}_l)^T$ represents $(\mathbf{I}_x \otimes \mathbf{M}_z^{-1} \mathbf{K}_z) \mathbf{U}$, and $\mathbf{B} = \mathbf{M}_z^{-1} \mathbf{K}_z$. Similarly, we obtain

$$(\mathbf{I}_x \otimes \mathbf{B}) \mathbf{U} = \bar{\mathbf{U}}, \quad (33)$$

which can be rewritten as

$$\begin{bmatrix} b_{11} & \cdots & b_{1n} \\ \vdots & \ddots & \vdots \\ b_{n1} & \cdots & b_{nn} \\ \vdots & & \ddots \\ b_{11} & \cdots & b_{1n} \\ \vdots & \ddots & \vdots \\ b_{n1} & \cdots & b_{nn} \end{bmatrix}_{l \times l} \begin{bmatrix} U_1 \\ U_2 \\ \vdots \\ U_l \end{bmatrix} = \begin{bmatrix} \bar{U}_1 \\ \bar{U}_2 \\ \vdots \\ \bar{U}_l \end{bmatrix}. \quad (34)$$

Matrix equation (34) is equivalent to a set of $n \times n$ matrix equations

$$\mathbf{B}\mathbf{U}^i = \bar{\mathbf{U}}^i, \quad (i = 1, 2, \dots, m), \quad (35)$$

where matrices $\mathbf{U}^i = (U_1^i, \dots, U_n^i)^T$ and $\bar{\mathbf{U}}^i = (\bar{U}_1^i, \dots, \bar{U}_n^i)^T$, ($i = 1, 2, \dots, m$), whose elements are along the z -direction, can be considered as a set of z -domain matrices of \mathbf{U} and $\bar{\mathbf{U}}$, respectively, corresponding to the point i in the x -domain. After some algebra, we implement the calculation of $\bar{\mathbf{U}}$ by solving the following multistep process:

$$\mathbf{M}_z \bar{\mathbf{U}}^i = \mathbf{K}_z \mathbf{U}^i. \quad (i = 1, 2, \dots, m). \quad (36)$$

With the approximate 1-D calculation through matrix equations (32) and (36), we obtain the value of $\mathbf{P}\mathbf{U}$:

$$\mathbf{P}\mathbf{U} = \bar{\mathbf{U}} + \bar{\mathbf{E}}. \quad (37)$$

We now discuss the solution of equation $(\mathbf{I} + \mathbf{P}_{x1})(\mathbf{I} + \mathbf{P}_{z1}) \mathbf{E}^{q+1} = \bar{\mathbf{E}}$, which can be represented by

$$\begin{aligned} & (\Lambda_{E1} + (\mathbf{M}_x^{-1} \mathbf{K}_x \otimes \mathbf{I}_z))(\mathbf{I} + \Lambda_{E1}^{-1} (\mathbf{I}_x \otimes \mathbf{M}_z^{-1} \mathbf{K}_z)) \mathbf{E}^{q+1} \\ & = \Lambda_{E1} \bar{\mathbf{E}}. \end{aligned} \quad (38)$$

Suppose $\bar{\mathbf{E}}^{q+1} = (\mathbf{I} + \Lambda_{E1}^{-1} (\mathbf{I}_x \otimes \mathbf{M}_z^{-1} \mathbf{K}_z)) \mathbf{E}^{q+1}$, equation (38) becomes

$$(\Lambda_{E1} + (\mathbf{M}_x^{-1} \mathbf{K}_x \otimes \mathbf{I}_z)) \bar{\mathbf{E}}^{q+1} = \bar{\mathbf{E}}, \quad (39)$$

where $\bar{\mathbf{E}} = \Lambda_{E1} \bar{\mathbf{E}}$. Equation (39) can be rewritten as

$$\begin{bmatrix} a_{11} + \Lambda_{E1,1} & \cdots & 0 & \cdots & a_{1m} & \cdots & 0 \\ \vdots & \ddots & \vdots & \cdots & \vdots & \ddots & \vdots \\ 0 & \cdots & a_{11} + \Lambda_{E1,n} & \cdots & 0 & \cdots & a_{1m} \\ \vdots & \vdots & \vdots & \ddots & \vdots & \vdots & \vdots \\ a_{m1} & \cdots & 0 & \cdots & a_{mm} + \Lambda_{E1,(m-1)n+1} & \cdots & 0 \\ \vdots & \ddots & \vdots & \cdots & \vdots & \ddots & \vdots \\ 0 & \cdots & a_{m1} & \cdots & 0 & \cdots & a_{mm} + \Lambda_{E1,l} \end{bmatrix}_{l \times l} \begin{bmatrix} \bar{E}_1^{q+1} \\ \bar{E}_2^{q+1} \\ \vdots \\ \vdots \\ \bar{E}_l^{q+1} \end{bmatrix} = \begin{bmatrix} \bar{\bar{E}}_1 \\ \bar{\bar{E}}_2 \\ \vdots \\ \vdots \\ \bar{\bar{E}}_l \end{bmatrix}, \quad (40)$$

where $\Lambda_{E1,j}$, \bar{E}_j^{q+1} , $\bar{\bar{E}}_j$, $j = 1, 2, \dots, l$, are elements of matrices Λ_{E1} , \bar{E}^{q+1} , and $\bar{\bar{E}}$, respectively. Matrix equation (40) is equivalent to a set of $m \times m$ matrix equations

$$(\bar{\Lambda}_k + \mathbf{A})\bar{\mathbf{E}}_k^{q+1} = \bar{\bar{\mathbf{E}}}_k, \quad (k = 1, 2, \dots, n), \quad (41)$$

where $m \times 1$ matrices $\bar{\Lambda}_k$, \bar{E}_k^{q+1} and $\bar{\bar{E}}_k$, $(k = 1, 2, \dots, n)$, whose elements are along the x -direction, can be considered as a set of x -domain matrices of Λ_{E1} , \bar{E}^{q+1} , and $\bar{\bar{E}}$, respectively, corresponding to the point k in the z -domain. After some algebra, we write matrix equation (41) as the following multi-step process

$$(\mathbf{M}_x \bar{\Lambda}_k + \mathbf{K}_x)\bar{\mathbf{E}}_k^{q+1} = \mathbf{M}_x \bar{\bar{\mathbf{E}}}_k, \quad (k = 1, 2, \dots, n) \quad (42)$$

Having obtained the value of \bar{E}^{q+1} with equation (42), we calculate \mathbf{E}^{q+1} through the following matrix equation

$$(\Lambda_{E1} + (\mathbf{I}_x \otimes \mathbf{M}_z^{-1} \mathbf{K}_z))\mathbf{E}^{q+1} = \bar{\bar{\mathbf{E}}}^{q+1}, \quad (43)$$

where $\bar{\bar{\mathbf{E}}}^{q+1} = \Lambda_{E1}\bar{\mathbf{E}}^{q+1}$. Equation (43) can be rewritten as

$$\begin{bmatrix} b_{11} + \Lambda_{E1,1} & \cdots & b_{1n} \\ \vdots & \ddots & \vdots \\ b_{n1} & \cdots & b_{nn} + \Lambda_{E1,n} \\ & & \ddots \\ & & b_{11} + \Lambda_{E1,(m-1)n+1} & \cdots & b_{1n} \\ 0 & & & \vdots & \vdots \\ & & & \ddots & \vdots \\ & & & \cdots & b_{nn} + \Lambda_{E1,l} \end{bmatrix}_{l \times l} \begin{bmatrix} E_1^{q+1} \\ E_2^{q+1} \\ \vdots \\ \vdots \\ E_l^{q+1} \end{bmatrix} = \begin{bmatrix} \bar{\bar{E}}_1^{q+1} \\ \bar{\bar{E}}_2^{q+1} \\ \vdots \\ \vdots \\ \bar{\bar{E}}_l^{q+1} \end{bmatrix}.$$

Matrix equation (44) is equivalent to a set of $n \times n$ matrix equations

$$(\bar{\Lambda}_i + \mathbf{B})\mathbf{E}_i^{q+1} = \bar{\bar{\mathbf{E}}}_i^{q+1}, \quad (i = 1, 2, \dots, m), \quad (45)$$

which can be written as the following multistep process:

$$(\mathbf{M}_z \bar{\Lambda}_i + \mathbf{K}_z)\mathbf{E}_i^{q+1} = \mathbf{M}_z \bar{\bar{\mathbf{E}}}_i^{q+1}, \quad (i = 1, 2, \dots, m), \quad (46)$$

where $n \times 1$ matrices $\bar{\Lambda}_i$, \mathbf{E}_i^{q+1} , and $\bar{\bar{\mathbf{E}}}_i^{q+1}$, $(i = 1, 2, \dots, m)$, whose elements are in the z -direction, can be considered as a set of z -domain matrices of Λ_{E1} , \mathbf{E}^{q+1} , and $\bar{\bar{\mathbf{E}}}^{q+1}$, respectively, corresponding to the point k in the z -domain.

We can achieve the multistep processes (32), (36), (42), and (46) through solving tridiagonal linear equations, each of which has the same orders corresponding to the 1-D FE matrix equation, e.g., the x -domain equation

$$(\mathbf{I}_x + \mathbf{P}_{x1})\mathbf{E}^{q+1} = (\mathbf{I}_x - \mathbf{P}_{x2})\mathbf{E}_x^q + \mathbf{R}_x^q, \quad (47)$$

which can be solved through the multistep process (32) at a given z -domain point $k \in (1, 2, \dots, n)$.

PERFORMANCE OF THE ALGORITHM

Efficiency analysis

The 1-D approximation algorithm breaks up the 2-D problem into a set of smaller subproblems that can be treated

$$\begin{bmatrix} E_1^{q+1} \\ E_2^{q+1} \\ \vdots \\ \vdots \\ E_l^{q+1} \end{bmatrix} = \begin{bmatrix} \bar{\bar{E}}_1^{q+1} \\ \bar{\bar{E}}_2^{q+1} \\ \vdots \\ \vdots \\ \bar{\bar{E}}_l^{q+1} \end{bmatrix}. \quad (44)$$

independently in every time step to decrease storage requirements and increase computational efficiency. The solution of every 2-D linear algebraic system in the FE matrix systems is achieved through solving $m+n$ linear algebraic systems with 1-D orders. Besides being easy to develop and code, the advantage of our approximation algorithm is that it significantly saves memory storage because the small 1-D coefficient matrices are employed instead of the large 2-D coefficient matrices.

Secondly, it significantly improves the performance of arithmetic operations and data access because the orders of linear algebraic systems are greatly reduced.

The efficiency of an algorithm decreases when solving a linear system nonlinearly because the size (or the number of nonzero elements) of the coefficient matrix increases. For example, solving a real-valued matrix equation with size N by the Gaussian elimination method requires an operation count of $O(N^3/3)$ when the coefficient matrix is full, or $O(Nb^2/2)$ when the coefficient matrix is banded with a semibandwidth of b . If a 2-D matrix equation system is directly processed using the Gaussian elimination method in the banded case, approximately $(m \times n) \times (n + 1)^2/2$ operations are required. But after our 1-D approximation, operations will reduce to $m \times n$ to solve $(m + n)$ corresponding 1-D systems using the same method. Of course, one can also reach similar results by using other well-known direct methods (e.g., the Gauss-Jordan algorithm) or iterative and time marching methods (e.g., the conjugate gradient method).

Furthermore, the 1-D approximation of the 2-D problem, creating explicitly uncoupled 1-D matrix equations, leads to an inherent high degree of parallelism in every time step. For example, matrix equation (32) consists of n independent systems of size m , while equation (36) likewise consists of m independent systems of size n . The 1-D system equations (32) and (36) can be efficiently performed in a parallel environment. A nonnumerical issue crucial to the performance of parallel computing is the frequency and cost of communication among processors and synchronization of those processors (Gentleman, 1978). In our case, the matrix equations are of the same order and completely decoupled between the unknowns in each direction. They can be solved in different processors synchronously without communication, resulting in efficient processor use in a parallel system. Moreover, the 1-D mass matrices are symmetric positive definite and strongly diagonal dominant so that no serious rounding error accumulates, i.e., the process of solving the 1-D systems is stable.

Approximation analysis

With functional analysis, we estimate the errors caused by substituting the matrix equation (28) for matrix equation (25). We define the relative errors as

$$\begin{aligned} E_r &= \frac{\|\mathbf{P}_{x1}\mathbf{P}_{z1}\|}{\|\mathbf{I} + \mathbf{P}_1\|} \\ &= \frac{\|(\Lambda_{E1}^{-1}(\mathbf{M}_x^{-1}\mathbf{K}_x \otimes \mathbf{I}_x))(\Lambda_{E1}^{-1}(\mathbf{I}_z \otimes \mathbf{M}_z^{-1}\mathbf{K}_z))\|}{\|\mathbf{I} + \Lambda_{E1}^{-1}(\mathbf{M}_x^{-1}\mathbf{K}_x \otimes \mathbf{I}_x) + \Lambda_{E1}^{-1}(\mathbf{I}_z \otimes \mathbf{M}_z^{-1}\mathbf{K}_z)\|}, \end{aligned} \quad (48)$$

where operator $\|\cdot\|$ is the Frobenius norm. The error is reliable for the time sampling rate dt , conductivity σ , grid spacing dx and dz , and the number of nodes.

Figure 1 presents the relation of the relative error with the factors mentioned above. As the time sampling rate dt increases, the relative error increases. As the conductivity σ , grid spacing dx and dz , and/or grid number increase, the relative error decreases. Figure 1 shows that if the mesh parameters and

material properties are given, we should use a smaller time sampling rate to obtain higher accuracy.

Comparison with the Green's function method

As a check of the numerical algorithm, we computed the high frequency electrical responses of a homogeneous whole-space ($\sigma = 0.01$ S/m) both with the approximate 1-D FE algorithm of equation (28) and with the analytical Green's function [equation (8)]. In this example, the main frequency of the impulsive function used in the numerical algorithm is 8 MHz.

The model for the numerical solution was of 1000 m in each direction with grid spacing of 20 m. The time step was 2×10^{-7} s. The electrical source was located at the center of the 2-D domain. The analytical and numerical results are plotted in Figure 2. As indicated in Figure 2(a), the agreement between the analytical and numerical solutions is satisfactory. Figure 2(b) shows the absolute errors, defined by $(E_{\text{computed}} - E_{\text{analytical}})$, and Figure 2(c) shows the relative errors defined by $100(E_{\text{computed}} - E_{\text{analytical}})/E_{\text{analytical}}$. The absolute and relative errors decrease with the time evolution of the field. The largest absolute error comes from the source location. Figure 2(c) shows that the relative errors are no more than 0.04% after 0.8 ms.

NUMERICAL SIMULATION

Our algorithm can deal with arbitrary complex models. But for illustration purposes and simplicity, we simulate two simple models to show the coevolution of the coupled seismic EM fields. The chosen geological material is a fully brine-saturated sandstone. The properties of the solid material and the fluid of the reservoir layer are the same as those of the confining layers. We assume the saturating brine has a conductivity of 2.0 S/m, a viscosity of 0.001 Pa·s and an electrolyte concentration of 0.001 mole/liter. The porosity, permeability and *SH* velocity of the confining layers are 4%, 0.01 D, and 3072 m/s, respectively. The porosity, permeability, and *SH* velocity of the reservoirs are 30%, 0.1 D, and 2187 m/s, respectively. We employ the Ricker wavelet function for seismic excitation. The dominant frequency of the wavelet is 20 Hz. Spatial and time sample rates are 15 m and 0.1 ms, respectively.

1-D model

This example shows the evolution of the *SH*-wave field and the EOS field in a 1-D model containing three geologic layers: first, a confining layer (500 m), then a reservoir (400 m), followed by another confining layer. At around 160 ms, the wavefront of the *SH*-wave arrives at the mechanical contrast (Figure 3a,b). We observe the transmitted and reflected *SH*-waves (Figure 3a) and an induced diffusive electric field (Figure 3c). The electric field propagates with a higher EM velocity in the confining layer and with a lower velocity in the reservoir than the *SH*-wave. It is strongly attenuated in the second layer where the conductivity is higher. When the *SH*-wave travels through the reservoir (160–340 ms), we can clearly see that there is a current sheet traveling with the mechanical *SH*-wave field (Figure 3c). The symmetry of the induced current sheet within the seismic pulse in the homogenous medium indicates that the seismic pulse does not radiate EM fields. When the *SH*-wave hits the second contrast at around

340 ms, we observe a weak electric field induced by a negative phase *SH*-wave.

2-D model

One of the key advantages of the FE approach to field computations is that the media can be described by full 2-D (even 3-D) distributions of parameters. This example shows the EOS conversion in a 2-D model (Figure 4) containing two reservoirs with complex structures which have the same mechanical and electrical properties for simplicity. For this model, snapshots (Figures 5–8), vertical EOS profiles (Figures 9 and 10) and surface (Figure 11) profiles are simulated to illustrate the coevolution of the seismic and EM fields.

Figure 5 shows snapshots of the solid displacement (a), relative fluid-solid displacement of the *SH*-wave (b), and the induced TE field (c) at time 220 ms. When the direct *SH*-wave arrives at the boundary of reservoir I, the seismic fields are disturbed at the interface, inducing the diffusive TE field. At the same time, there is a weak disturbance around reservoir II although the seismic wave has yet to reach there. It is in-

duced by the TE field from the reservoir I because the TE field diffuses much faster than the seismic field. The conversion of seismic to electromagnetic energy always accompanies the seismic propagation in porous media, but EM fields occur only at the medium contrasts.

Figure 6 shows snapshots of the solid displacement (a), relative fluid-solid displacement of the *SH*-wave (b), and the induced TE field (c) at time 366 ms when the direct *SH*-wave arrives at the boundary of reservoir II. The direct seismic field now senses the existence of reservoir II. At the same time, diffracted seismic waves are propagating in reservoir I, inducing diffusive TE fields around reservoir I. The EM fields from both reservoirs are superposed because of their high travelling speed. But the direct wave still dominates. As a result, the direct wave is the main cause to the conversion.

At time 600 ms, when the direct *SH*-wave has passed through the bottom of reservoir II (Figure 7), the transmitted wave, multiple wave, and diffracted wave in reservoir II interact with each other and generate complex EM fields. At the same time, TE fields are also induced from reservoir I due to the reflected seismic waves from reservoir II. In this situation, it is difficult to

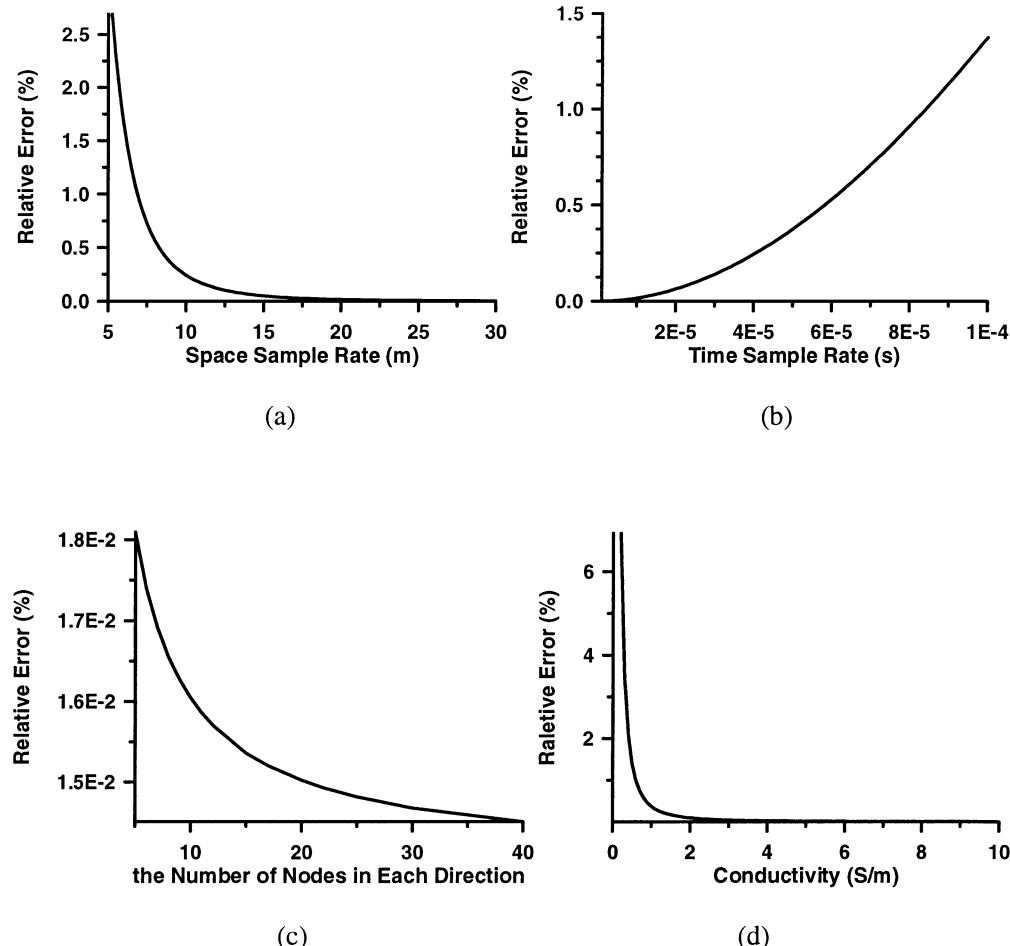


FIG. 1. Errors caused by substituting matrix equation (28) for equation (25): (a) relative error versus the space sampling rate ($dx = dz$) with $dt = 10^{-5}$ ms, $N_x = N_z = 10$, and $\sigma = 1.0$ S/m; (b) relative error versus the time sampling rate Δt with $dx = dz = 20$ m, $N_x = N_z = 10$, and $\sigma = 1.0$ S/m; (c) relative error versus the grid number in each direction ($N_x = N_z$) with $dx = dz = 20$ m, $dt = 10^{-5}$ ms, and $\sigma = 1.0$ S/m; (d) relative error versus the conductivity of the brine-saturated porous rock with $dt = 10^{-5}$ ms, $N_x = N_z = 10$, and $dx = dz = 20$ m.

distinguish the two reservoirs from observed EM data because of interference.

Figure 8 shows the snapshots at time 888 ms. No direct *SH*-wave can be observed at this time. The transmitted wave, multiple wave, reflected wave, and diffracted wave interact, dominate, and generate complex superposed diffusive electric fields around reservoir I and reservoir II. The complexity may result in difficulties in interpreting the EOS data.

Obviously, direct seismic waves are desired and should be used in EOS applications. Compared with other waves, direct

waves have simple distribution patterns and high energy during traveling in heterogeneous media. EM signals resulted from direct waves can be easily recognized since they dominate all the induced fields. As a result, reservoir information (e.g., structure) can be easily obtained from the strong EM signals.

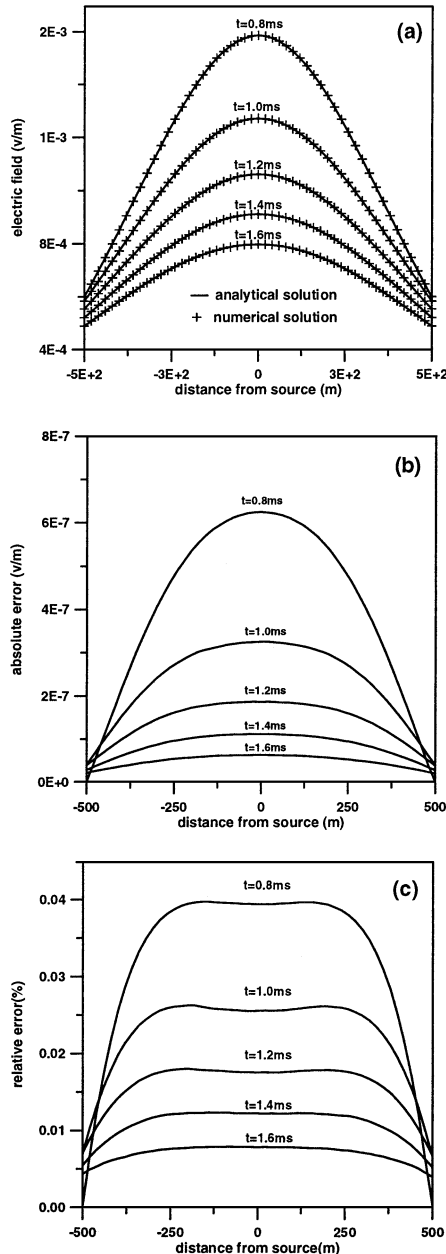


FIG. 2. Accuracy analysis. The electrical fields are excited by a line source at the origin on the 2-D conductive whole space ($\sigma = 0.01 \text{ S/m}$). Profiles are at 0.8, 1.0, 1.2, 1.4, and 1.6 ms. (a) Comparison between analytical (solid line) and numerical (cross) solutions. (b) Absolute errors of the FE solution. (c) Relative errors of the FE solution.

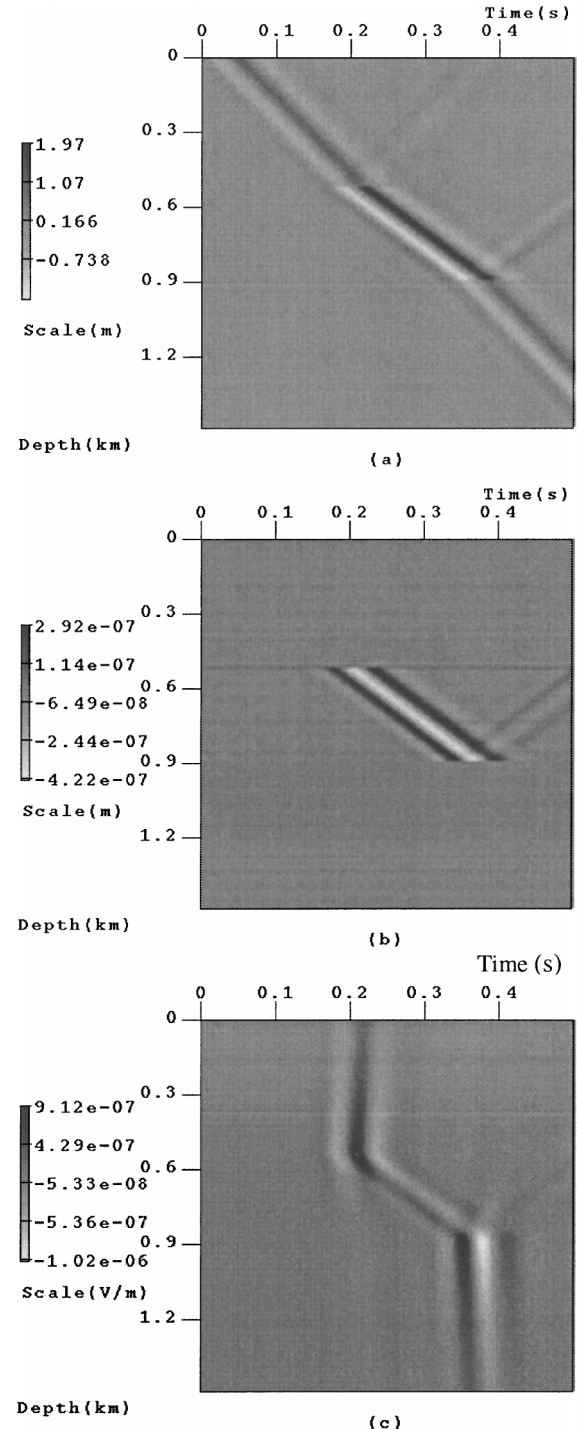


FIG. 3. Synthetic snapshots of the matrix displacement for the 1-D model. Time axis shows the 1-D snapshots at different time. The depth axis shows the distance of the *SH*-wave propagation from the source at the origin; (a) displacement of the frame rock, (b) displacement of the fluid relative to the solid, (c) induced electric field.

Figure 9 shows the simulated common source EOS surface survey data. The TE response of the lower reservoir is much weaker than that of the upper reservoir due to electrical and seismic attenuation. The EM signals arrive at the antennas very early, approximately one half of the time for the seismic wave because of the high diffusive speed of the EM fields.

Figures 10 and 11 show vertical seismic profiles from the wells at horizontal distances of 600 and 900 m, respectively. In Figure 10, the maximum value of the TE field response from the upper reservoir is approximately equal to that from the lower reservoir because well I has penetrated both reservoir I and reservoir II. Figure 11 shows that the maximum value of the TE response from the lower reservoir is much larger than that from the upper reservoir because well II has only penetrated the lower reservoir. Part of the energy of the TE field is lost because of its attenuation and spreading. The diffusive nature of the induced EM field suggests that antennas should be positioned close to the target of interest. Thus, in applications to reservoir characterization, borehole, instead of surface, EOS surveys should be used.

DISCUSSION AND CONCLUSIONS

The approximate 1-D algorithm of the FE method for the coupled *SH*-wave and TE field equations saves large amounts of computational time and storage. The processes of solving the FE matrix equations in every multistep process are parallel so that the new FE algorithm is more efficient when it is implemented on a vector or parallel computer. The memory storage requirements are only of the same order of the unknown vector. The basis functions used in our algorithm are of first order, although higher order polynomial basis functions are also feasible for the algorithm. The 2-D coefficient matrices can be decomposed into a set of 1-D matrices so that the 2-D FE matrix equations can be solved through the approximate 1-D FE algorithm. In these cases, the systems of the approximate 1-D FE matrix equations are no longer tridiagonal but pentadiagonal, septadiagonal, etc. Therefore the advantages

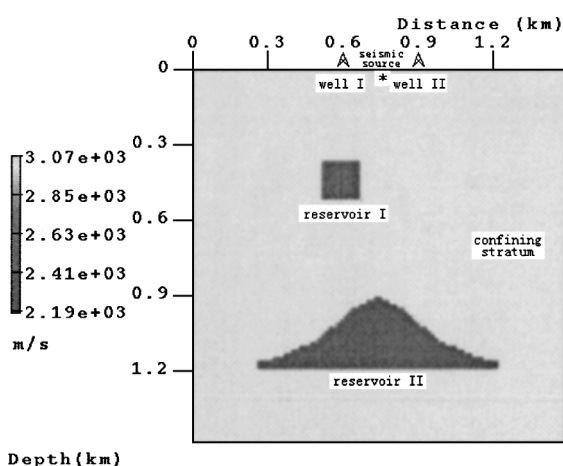


FIG. 4. Geometry of the 2-D EOS model containing two reservoirs with the same mechanical and electrical properties. The saturating brine has a conductivity of 2.0 S/m, a viscosity of 0.001 Pa·s and an electrolyte concentration of 0.001 mole/liter. The porosity, permeability and *SH* velocity of the confining layers are 4%, 0.01 D, and 3072 m/s, respectively. The porosity, permeability, and *SH* velocity of the reservoirs are 30%, 0.1 D, and 2187 m/s, respectively.

mentioned earlier should be even more attractive because the coefficient matrices possess more nonzero elements. The idea of 1-D approximation can also be applied to some 3-D problems. At present, our algorithm only works with regular grids. When the grids are irregular, our algorithm will have to be modified.

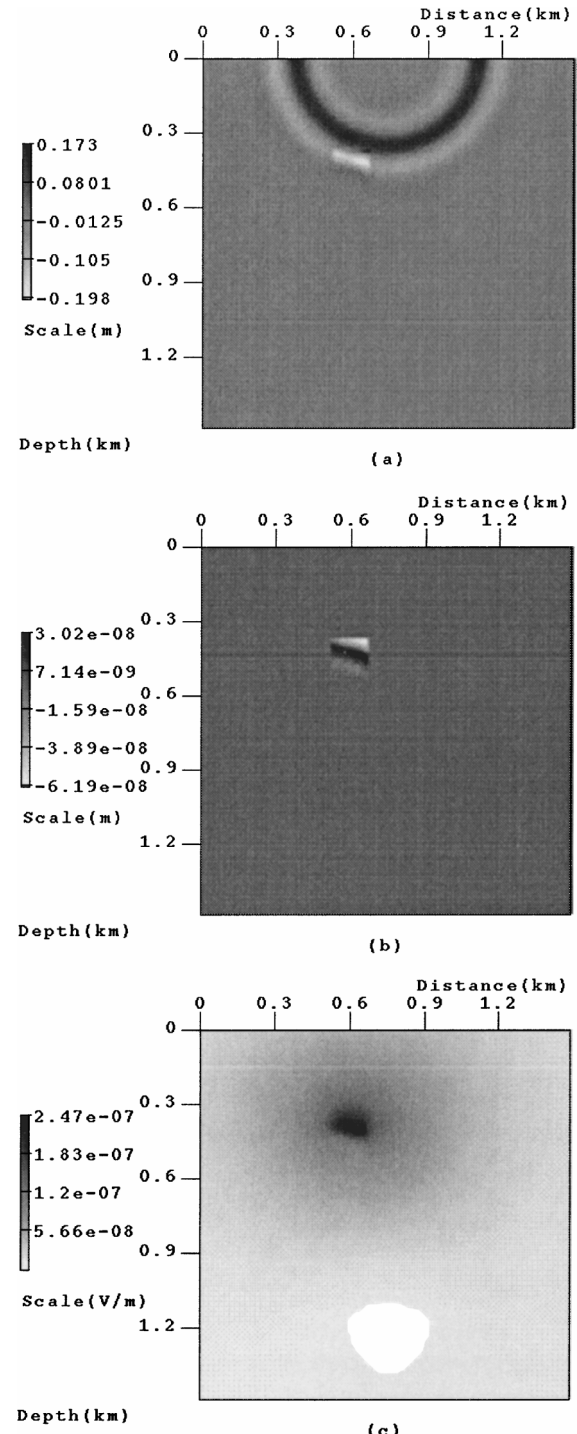
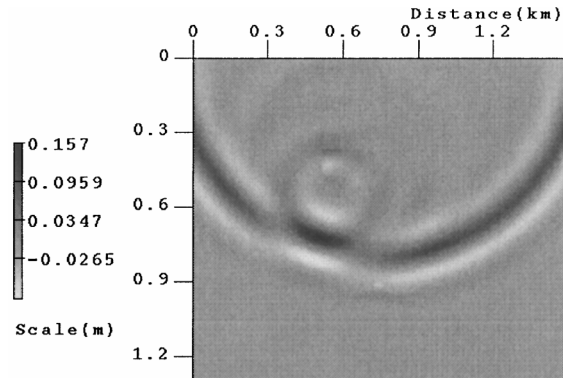
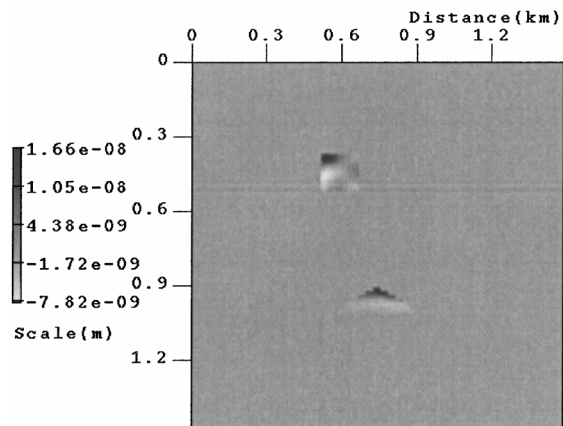


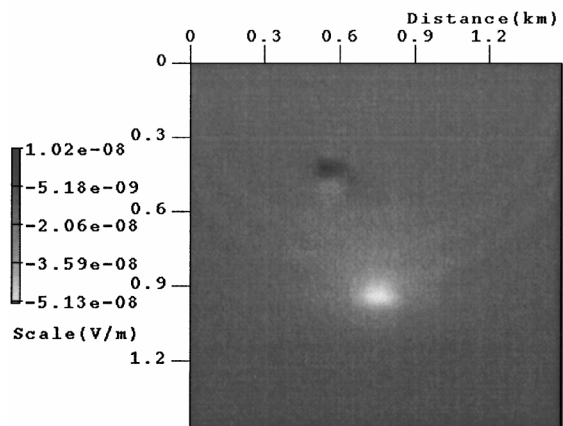
FIG. 5. Snapshots of the solid displacement (a), relative fluid-solid displacement of the *SH*-wave (b), and the induced TE field (c) at 220 ms. The seismic fields are disturbed due to the singularity of the media. The diffusive TE field from reservoir I forms due to the imbalance of the induced electric current.



(a)

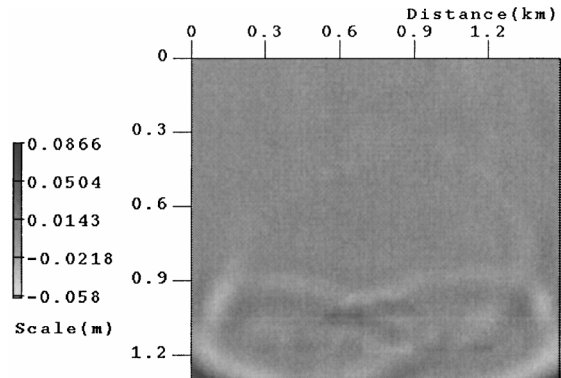


(b)

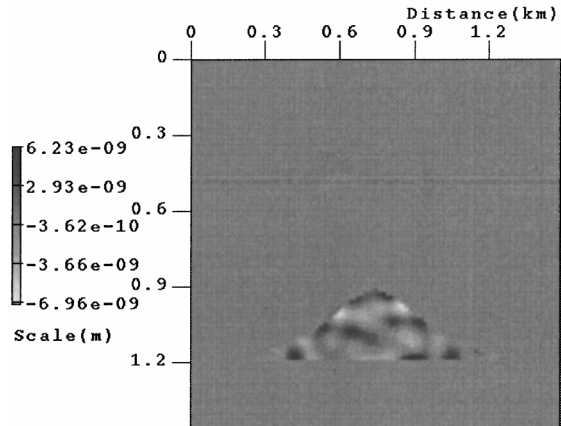


(c)

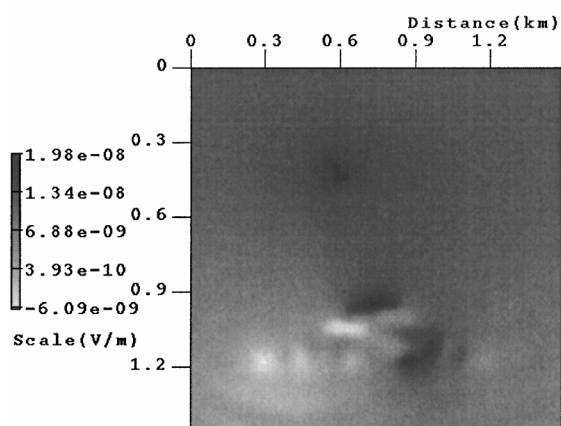
FIG. 6. Snapshots of the solid displacement (a), relative fluid-solid displacement of the SH -wave (b), and the induced TE field (c) at 366 ms. When the direct SH -wave arrives at the boundary of reservoir II, the direct seismic fields are disturbed because of the existence of reservoir II. Meanwhile, diffracted seismic waves are moving around reservoir I, inducing diffusive TE fields in reservoir I that is caused by the imbalance of the induced electrical current.



(a)



(b)



(c)

FIG. 7. Snapshots of the solid displacement (a), relative fluid-solid displacements of the SH -wave (b), and the induced TE field (c) at 600 ms. When the direct SH -wave has passed through the bottom of reservoir II, the transmitted wave, multiple wave, and diffracted wave are inducing the diffusive electric field around reservoir II. Meanwhile, a TE field is also induced from reservoir I due to the reflected seismic wave from reservoir II.

The algorithm we developed can be used to simulate complex EOS phenomena in heterogeneous porous media and to guide data acquisition, processing, and interpretation. With the FE method, we have simulated 1-D and 2-D *SH*-TE

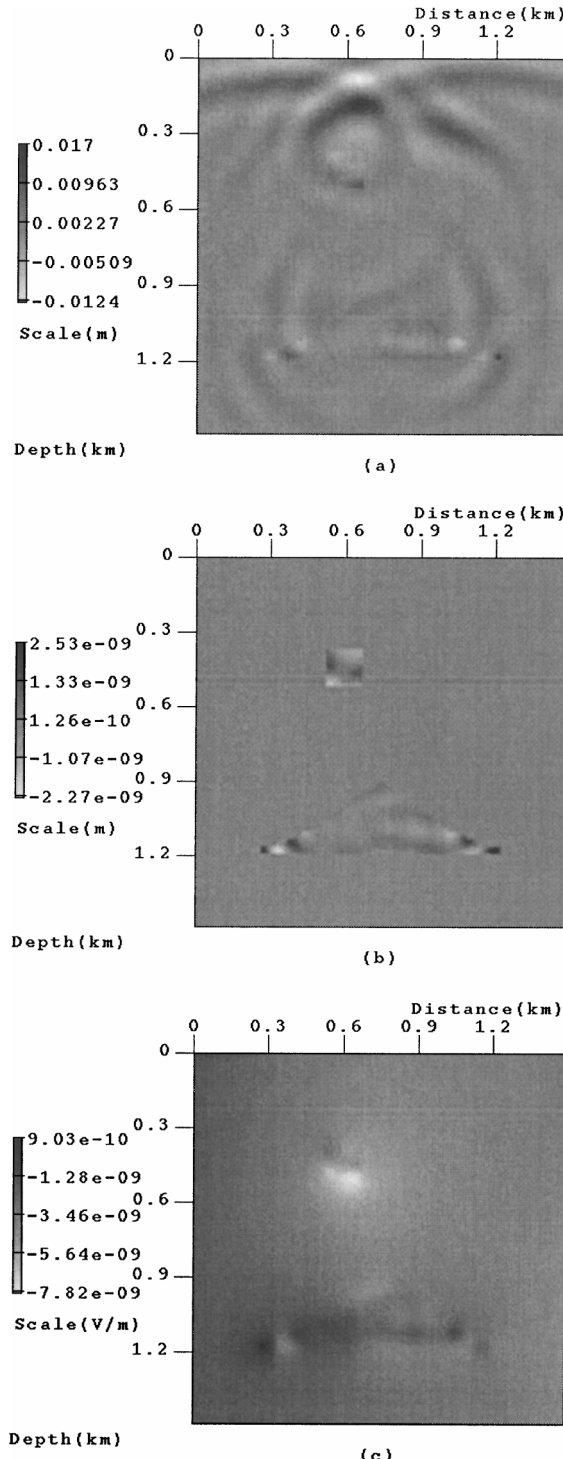


FIG. 8. Snapshots of the solid displacement (a), relative fluid-solid displacements of the *SH*-wave (b), and the induced TE field (c) at 888 ms. Transmitted wave, multiple wave, reflected wave, and diffracted wave are all present in the area, inducing superposed diffusive electric fields around reservoirs I and II. The complexity of the seismic wave field results in difficulties for EOS data interpretation.

EOS fields. The diffusive electrical field may be induced at the mechanical or chemical contrasts. The induced electrical current accompanies the seismic wave when traveling in the electrolyte-saturated porous medium. Conductive media decrease the converted electric response considerably both in the wells and at the surface. For deep reservoir applications, we should pay more attention to borehole EOS methods.

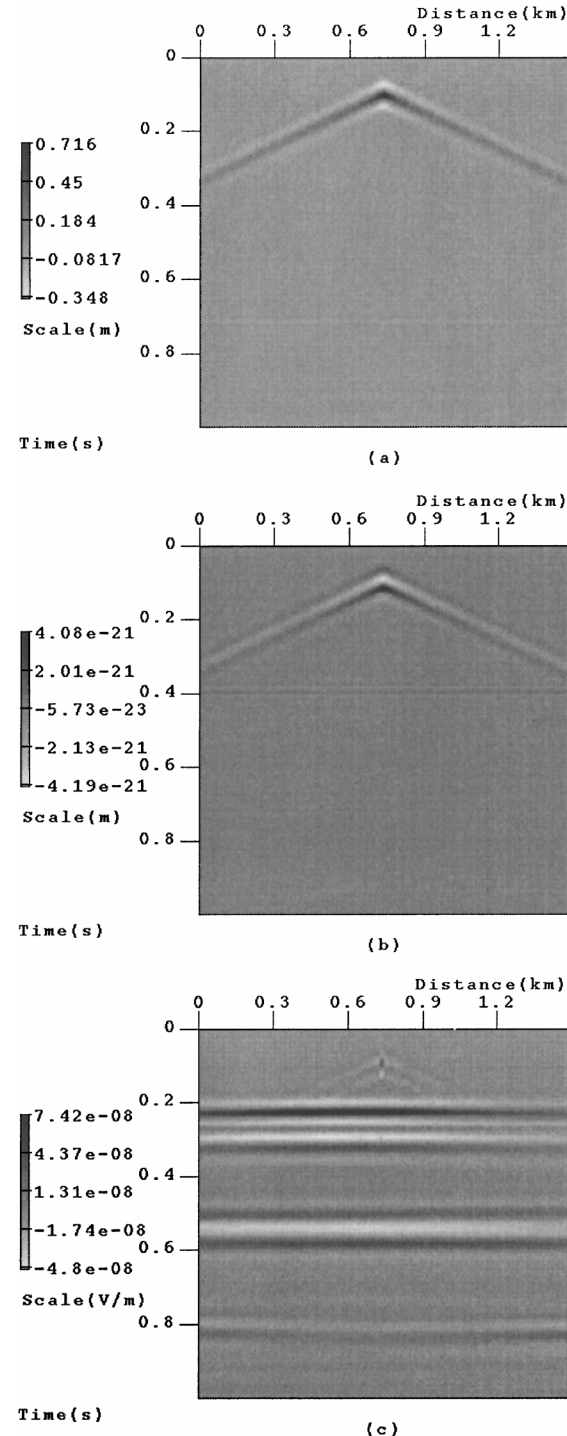


FIG. 9. Common source surface survey electric data. The TE response of the lower reservoir is much weaker than that of the upper reservoir because of the electric and the seismic attenuation in the porous media.

Complex seismic field patterns result in complex EM field patterns, leading to difficulties in interpreting the induced EM data. Although there is no obvious superiority in resolution and simplicity for the induced EM data over seismic data, the EOS conversion mechanism might be useful in reservoir characterization because it has a close relation to the reservoir parameters especially the permeability. In this paper, we only simulated a set of simple reservoir parameters to test our algorithm. Further work should be carried out using the method presented here to understand the EOS phenomena in more realistic environments. For instance, the contribution of

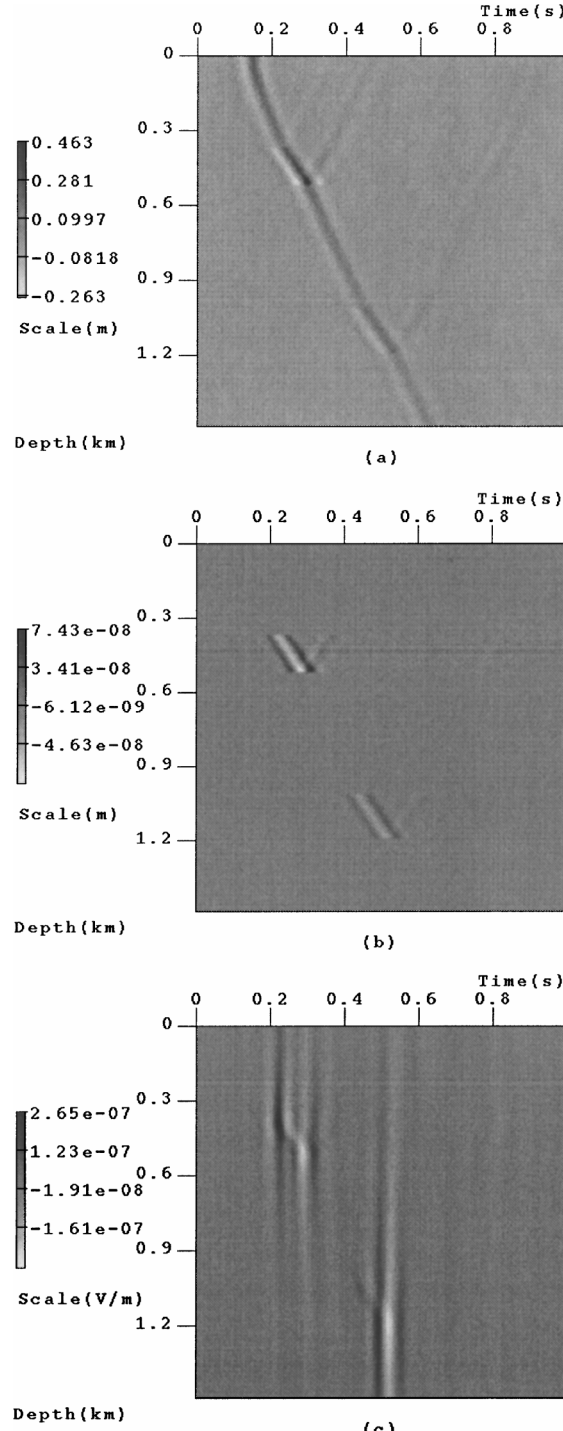


FIG. 10. Vertical seismic profiles (a and b) and TE field profile (c) from well I. The maximum value of the TE field response from the upper reservoir is approximately equal to that from the lower reservoir because well I has penetrated both reservoirs I and II.

part of the energy of the TE field is lost because of its attenuation.

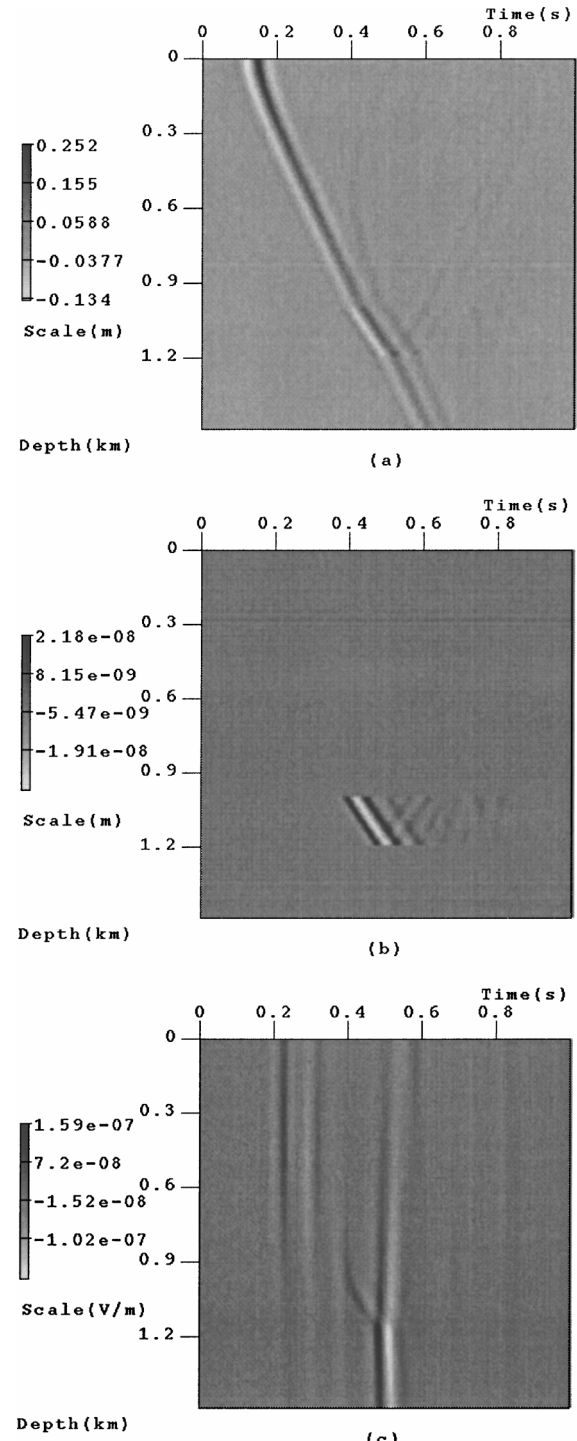


FIG. 11. Vertical seismic profiles (a and b) and TE field profile (c) from well II. The maximum value of the TE response from the lower reservoir is much larger than that from the upper reservoir because well II has only penetrated the lower reservoir. Part of the energy of the TE field is lost because of its attenuation.

mechanical and electromagnetic contrasts to the conversion in real media should be further understood. In addition, the method should be extended to 3-D full wavefield cases, which would be a very challenging task.

ACKNOWLEDGMENTS

The research project “Electroseismic Effects in Oil/Gas Reservoirs” is sponsored by the Shandong Science Foundation. We thank David Boerner, Ian Kay, and an anonymous reviewer for their constructive reviews and suggestions.

REFERENCES

- Archie, G. E., 1942, The electrical resistivity log as an aid in determining some reservoir characteristics: *Trans. AIME*, **146**, 54–62.
- Berryman, J. G., 1980, Long-wavelength propagation in composite elastic media, I. Spherical inclusions: *J. Acoust. Soc. Am.*, **68**, 1809–1819.
- Biot, M. A., 1956, Theory of propagation of elastic waves in a fluid-saturated porous solid. I. Low-frequency range: *J. Acoust. Soc. Am.*, **28**, 179–191.
- , 1962, Mechanics of deformation and acoustic propagation in porous media: *J. Appl. Phys.*, **33**, 1482–1498.
- Blau, L. W., and Statham, L., 1936, Methods and apparatus for seismic electric prospecting: US Patent 2 054 067.
- Bockris, J., and Reddy, A. K. N., 1970, Modern electrochemistry: Plenum Press.
- Dukhin, S., and Derjaguin, B. V., 1974, Surface and colloid science: Wiley-Interscience.
- Fitterman, D. V., 1978, Electrokinetic and magnetic anomalies associated with dilatant regions in a layered earth: *J. Geophys. Res.*, **83**, 5923–5928.
- Frenkel, J., 1944, On the theory of seismic and seismoelectric phenomena in a moist soil: *J. Physics (Soviet)*, **8**, 230–241.
- Gentleman, W., 1978, Some complexity results for matrix computations on parallel processors: *J. ACM*, **25**, 112–115.
- Goldman, Y., Hubans, C., Nicoletis, S., and Spitz, S., 1986, A finite-element solution for the transient EM response of an arbitrary two-dimensional resistivity distribution: *Geophysics*, **51**, 1450–1461.
- Gu, X., 1985, Modeling in frequency domain with the finite-element method: *Geophysical Prospecting for Petroleum*, **24**, 44–49 (in Chinese).
- Han, Q., 1995, The electroseismic effect in porous media: a new method for exploration of oil/gas reservoirs: Univ. of Petroleum Press, 195–197 (in Chinese).
- , 1997, Electroseismic wave equations in fluid-saturated porous media: *Geophysical Prospecting for Petroleum*, **36** (Sup.), 14–19 (in Chinese).
- Ivanov, A., 1939, Effect of electrization of earth layers by elastic waves passing through them: *Comptes Rendus (Doklady) de l'Academie des Sciences de l'USSR*, **24**, 42–45.
- Lu, J., and Guan, Z., 1987, Numerical schemes for solving partial differential equations: Qinghua Univ. Press (in Chinese).
- Marfurt, K. J., 1984, Accuracy of finite-difference and finite-element modeling of the scalar and elastic wave equations: *Geophysics*, **49**, 533–549.
- Martner, S., and Sparks, N., 1959, The electroseismic effect: *Geophysics*, **24**, 297–308.
- Mikhailov, O. V., Haartsen, M. W., and Toksöz, M. N., 1997, Electroseismic investigation of the shallow subsurface: Field measurements and numerical modeling: *Geophysics*, **62**, 97–105.
- Oristaglio, M. L., and Hohmann, G. W., 1984, Diffusion of electromagnetic fields into a two-dimensional earth: A finite-difference approach: *Geophysics*, **49**, 870–894.
- Parkhomenko, E. I., 1971, Electrification phenomena in rocks: Plenum Press.
- Pratt, R. G., 1990, Frequency-domain elastic wave modeling by finite differences: A tool for crosshole seismic imaging: *Geophysics*, **55**, 626–632.
- Pratt, R. G., and Worthington, M. H., 1990, Inverse theory applied to multi-source cross-hole tomography. Part I: Acoustic wave-equation method: *Geophys. Prosp.*, **38**, 287–310.
- Pride, S. R., 1994, Governing equations for the coupled electromagnetics and acoustics of porous media: *Phys. Rev.*, **B50**, 15 678–15 696.
- Pride, S. R., and Haartsen, M. W., 1996, Electroseismic wave properties: *J. Acoust. Soc. Am.*, **100**, 1301–1315.
- Pride, R. S., and Morgan, F. D., 1991, Electrokinetic dissipation induced by seismic waves: *Geophysics*, **56**, 914–925.
- Song, Z.-M., and Williamson, P. R., 1995, Frequency-domain acoustic-wave modeling and inversion of crosshole data: Part I—2.5-D modeling method: *Geophysics*, **60**, 784–795.
- Sprunt, E. S., Maute, R. E., and Rackers, C. L., 1990, An interpretation of the SCA electrical resistivity study: *The Log Analyst*, **31**, 76–88.
- Thompson, A. H., and Gist, G. A., 1993, Geophysical applications of electrokinetic conversion: *The Leading Edge*, **12**, 1169–1173.
- Thompson, R. R., 1936, The seismic electric effect: *Geophysics*, **1**, 327–335.
- Thompson, R. R., 1939, A note on the seismic electric effect: *Geophysics*, **4**, 102–105.
- Wolf, K. B., 1979, Integral transforms in science and engineering: Plenum Press, New York.